RSC Advances

PAPER

View Article Online
View Journal | View Issue

Cite this: *RSC Adv.*, 2026, **16**, 9817

Enhancing the electrochemical performance of trimetallic sulfide through metal-oxide nanocomposite engineering for high-performance supercapacitors

Muhammad Tariq,[a] Mohsin Ali Marwat, †*[a] Areeba Sajid,[a] Anusha Arif,[a] Zuhair Ehsan,[a] Muhammad Ramzan Abdul Karim[a] and Syed Shaheen Shah[bc]

Supercapacitors, considered a potential energy storage device, can address the long-awaited problem of the energy crisis by storing energy for efficient, rapid, and sustainable utilization across diverse applications, from portable electronics to large-scale power systems. Herein, we have prepared a novel nanocomposite material *via* a novel ultrasonication-assisted solvothermal approach, combining the $Fe_{0.67}Cu_{0.22}Co_{0.11}S$ nanoparticles and CuO in different weight ratios. X-ray diffraction, scanning electron microscopy, and Fourier transform infrared spectroscopy analyses confirmed the successful synthesis of the targeted nanocomposites. Electrochemical evaluation revealed that the FeCuCoS/CuO 5 : 1 composition (denoted as U5), identified as optimal material, exhibited a remarkable specific capacitance of 1407 F g^{-1} at 0.7 A g^{-1}, corresponding to enhancements of 3.9-fold and 120-fold compared to pristine $Fe_{0.67}Cu_{0.22}Co_{0.11}S$ and CuO, respectively. Furthermore, the asymmetric supercapacitor device based on U5 demonstrated superior electrochemical performance, delivering a specific capacity of 311 C g^{-1} at 0.5 A g^{-1}, an energy density of 70 Wh kg^{-1}, a power density of 4800 W kg^{-1}, a coulombic efficiency of 97.1%, and a long-term cycling stability of 92.86% after 3000 cycles. Dunn's model analysis indicated that charge storage was predominantly capacitive (51.3% at 10 mV s^{-1}), while power-law fitting yielded *b*-values of 0.71–0.80, indicating hybrid supercapacitor behavior. Overall, $Fe_{0.67}Cu_{0.22}Co_{0.11}S$/CuO nanocomposites demonstrated durable, high-performance characteristics for advanced energy storage applications.

Received 21st November 2025
Accepted 8th January 2026

DOI: 10.1039/d5ra09004k

rsc.li/rsc-advances

1 Introduction

The increasing demand for portable electronics, power systems, electric vehicles, and the integration of sustainable energy sources has generated growing interest in green and smart energy solutions and innovations.[1–4] In addition, to address Sustainable Development Goal (SDG) number 7, *i.e.*, affordable and clean energy, scientists around the world are searching for powerful energy storage solutions that have the utmost capability to store charge rapidly and deliver the stored energy efficiently whenever it is required. To address this challenge, supercapacitors are considered as one of the potential energy storage devices, as they effectively bridge the performance gap between conventional capacitors, which deliver the highest power densities but suffer from lower energy densities, and rechargeable batteries, which offer higher energy densities but lack the higher power densities, slow reaction kinetics and short cycling stability.[5,6] Supercapacitors, having both non-faradic (capacitive nature) and faradaic (diffusive nature) reactions during oxidation and reduction, can overcome the aforementioned problems by taking the advantage of high power density from its capacitive nature while an advantage of optimal energy density from its diffusive nature, making them an ideal energy storage solution for the applications that require fast energy transference and long cycling stability.[7,8] In addition, supercapacitors offer advantages such as a wide operating temperature range, high coulombic efficiency, environmental friendliness, and reliability.[9–12] Supercapacitors are commonly categorized as hybrid, electric double-layer capacitors (EDLCs), and pseudocapacitors supercapacitors.[13,14] Hybrid supercapacitors combine both non-faradic and faradaic reactions; EDLCs rely on non-faradic reactions, and pseudocapacitors rely on faradaic reactions.[15] Recently, hybrid supercapacitors have attracted much attention and are extensively researched because of their high power and energy densities, resulting from non-faradic and faradaic reactions, respectively.[16–20] In the

[a]*Faculty of Materials and Chemical Engineering, Ghulam Ishaq Khan (GIK) Institute of Engineering Sciences and Technology, Topi, 23640, Pakistan. E-mail: mohsin.ali@giki.edu.pk; Fax: +92-938-281032; Tel: +92-938-281026*

[b]*Renewable Energy and Environmental Technology Center, University of Tabuk, Tabuk 47913, Saudi Arabia*

[c]*Department of Physics, Faculty of Science, University of Tabuk, Tabuk 47913, Saudi Arabia*

† Equal contribution.

literature, electrode materials, considered one of the major parameters governing supercapacitor performance, have received extensive research focused on conducting polymers,[21] transition metal oxides,[22] carbon-based materials,[23] and, more recently, transition metal sulfides.[24] Among these, sulfide-based electrodes are particularly promising because of their superior electrical conductivity, rich redox activity, and ability to facilitate rapid ion transport, which collectively enhance both the specific capacitance and energy density of supercapacitors.[25]

The research community examining supercapacitors, due to their high specific capacitance and global accessibility and viability, favors transition-metal-sulfide (TMS) supercapacitors based on Fe, Co, Ni, Bi, Cu, and Cd.[26,27] Moreover, their conductivity is much higher than that of hydroxides and oxides.[28,29] Fe-based Co–Cu doped sulfides, amongst various TMS-based supercapacitors, yield an intense conductive and stable sulfide,[30] which is one of the major characteristics expected from such supercapacitors. They also show fast faradaic redox reactions, show combined effects of constituents transition metal sulfides, and possess high theoretical capacitance.[31,32] Studies have shown that TMS-based electrodes achieved outstanding electrochemical performance and enhanced capacitive properties *via* the following approaches: morphological control and composite engineering.[33] To date, there are very few literature reports on trimetallic TMS of the type Fe–Cu–Co for energy storage applications;[15] thus, the current focus in supercapacitor technology is on TMS, especially those based on Fe, Co, and Cu as electrode materials.[34] An appropriate combined pathway in a multicomponent composite can enhance the conductivity of both ions and electrons, thereby improving the overall energy storage capability of TMS electrodes.[35] Binary and ternary TMS systems perform better than unary TMS due to their good conductance, high electrochemical stability, and the synergy that emerges from interactions among the transition metals, resulting in improved specific capacity, cycling stability, and efficiency.[17,36]

Apart from the advantages, there are some concerns related to the utilization of TMS in supercapacitor applications, such as slow ion transportation, loss of structural integrity from volume changes, and extremely poor intrinsic electrical conductivity after a number of cycles.[37] Together, these factors cause poor synergistic performance and fast capacity loss from the electrode materials.[38,39] To address these issues, researchers have been investigating various conductive materials, including carbonaceous materials (graphene, carbon nanotubes (CNTs), and quantum dots),[40,41] conductive polymers (polypyrrol and polyaniline),[42,43] or advanced nanoarchitectures for achieving an improved electrochemical characteristic supercapacitor electrode materials. Copper-based nanomaterials, due to their distinct electrochemical characteristics, are one of the most appropriate conductive materials, showing ease in functionalization, having a high surface area, and demonstrating high electrical conductivity.[44] Further, it can be used with TMS-based electrode materials or possibly composited with other electrically and ionically conductive nanomaterials to create highly efficient asymmetric supercapacitors. Nevertheless, approaches such as morphology control, doping, and surface modification alone cannot overcome these challenges. Therefore, composite engineering stands out as a better option, ensuring improved structural stability and reliable electrochemical performance over extended cycles.[45] Copper oxide, on one hand, is an important additive that promotes supercapacitor electrode performance mainly by improving the overall composite morphology and improving conductivity.[46] It acts as a chelating agent during synthesis, controlling the growth of nanostructures toward uniform, porous, and high-surface-area morphologies: nanosheets or flower-like structures. Such characteristics are very helpful for electrolyte penetration and ion diffusion, which are paramount for efficient charge storage.[47] Furthermore, copper citrate can also act as a precursor for conductive copper or carbon-containing phases, both of which, in turn, promote electron transport within the electrode material. The ability of copper citrate to promote structural development while at the same time enhancing the electrical conductivity renders it a worthy additive to create materials for high-performance electrodes.[48]

Moreover, the incorporation of copper oxide (CuO) into TMS-based nanomaterials offers a promising strategy to enhance the overall conductivity of the composite material, thereby expanding its potential for supercapacitor applications. Although TMS is a well-known semiconductor, its relatively low conductivity often limits its practical performance. By integrating CuO, an interconnected and relatively higher electrically conductive network can be established, where well-dispersed CuO nanoparticles create percolation pathways that facilitate efficient electron transport and mitigate the intrinsic resistive nature of TMS.[49,50] Furthermore, the heterointerface between TMS and CuO promotes enhanced charge transfer, as the presence of CuO can modify the electronic band structure of the composite, reduce the energy band gap, and introduce favorable energy states for carrier mobility. Beyond these improvements, synergistic interactions between the two phases may induce the formation of new structures, such as chalcopyrite ($CuFeS_2$), which possess superior electrical characteristics compared to the individual components.[51] This cooperative effect underscores the potential of TMS/CuO composites as advanced functional materials for next-generation energy devices. Using similar motivation, we prepared a novel $Fe_{0.67}Cu_{0.22}Co_{0.11}S$/CuO nanocomposite electrode material, which showed an outstanding specific capacitance of 1407 F g^{-1}. In addition, its asymmetric supercapacitor device indicated an extraordinary energy density of 70 Wh kg^{-1}, power density of 4800 W kg^{-1}, a coulombic efficiency of 97.1%, and cycling stability of 92.86% after 3000 cycles. Moreover, Dunn's model analysis indicated that charge storage was predominantly capacitive, and power-law fitting signified its hybrid supercapacitor nature.

2 Experimental

2.1 Materials

Copper(II) chloride dihydrate ($CuCl_2 \cdot 2H_2O$; ≥99.0%), cobalt(II) chloride hexa-hydrate ($CoCl_2 \cdot 6H_2O$; 98%), iron(III) chloride trihydrate ($FeCl_3 \cdot 3H_2O$; ≥99%), acetylene black (AB; 98%),

potassium hydroxide (KOH; 99.995%), sodium sulfide nonahydrate ($Na_2S \cdot 9H_2O$; ≥99.99%), n-methyl 2-pyrrolidone (NMP; 99.5%), and polyvinylidene fluoride (PVDF; average M_w ~534 000 by GPC), acetone (99.5%) were obtained from Sigma-Aldrich Nickel foam, used as a substrate, was procured from Pi-Kem, Tamworth, UK; sodium citrate ($Na_3C_6H_5O_7$, ≥99%) and copper nitrate ($CuNO_3$, ≥99%) were also obtained from the same supplier and were used without modification. The experimental procedure also involved Sigma-Aldrich's polyethylene glycol (PEG; molecular weight = 6000, Molecular Biology Grade), deionized (DI) water, and ethanol (99.5%). A 100 mL stainless-steel autoclave, procured from a local vendor, was used for performing hydrothermal synthesis. The reference electrode was a mercury electrode made of Hg/HgO, while a counter electrode of a platinum disc, used in the electrochemical analysis, was procured from Sigma-Aldrich.

2.2 Synthesis of $Fe_{0.67}Cu_{0.22}Co_{0.11}S$

To prepare the $Fe_{0.67}Cu_{0.22}Co_{0.11}S$ nanomaterial (U1), 7.20 g of $Na_2S \cdot 9H_2O$, 0.785 g of $CoCl_2 \cdot 6H_2O$, 1.125 g of $CuCl_2 \cdot 2H_2O$, and 2.909 g of $FeCl_3 \cdot H_2O$ were weighed accurately. Each precursor was separately dissolved and stirred for 30 minutes in a polyethylene glycol-mixed deionized (DI) water solution of 20 mL to ensure its complete dissolution. The prepared solutions were then combined, following the sequence shown in Fig. 1(a), and continuously stirred for an additional 1 hour. A hydrothermal treatment at 180 °C for 6 hours was conducted by transferring the as-prepared homogenous solution into a 100 mL Teflon-lined stainless-steel autoclave. Later, the product/nanoparticles were collected by a method called centrifugation for 10 minutes at 6000 rpm. The as-obtained nanoparticles were subjected to washing several times with methanol, acetone, and DI water, and under the same centrifugation conditions to remove residual impurities. The cleaned material was then dried in a vacuum oven at 60 °C for 12 hours. Finally, the dried powder underwent annealing at 300 °C for 3 hours in an argon atmosphere, producing crystalline $Fe_{0.67}Cu_{0.22}Co_{0.11}S$ (U1), see Fig. 1(a).[52]

2.3 Synthesis of copper citrate

As shown in Fig. 1(b), a detailed schematic process of the synthesis of copper citrate is presented. It involved the dissolution of 1 g of $CuNO_3$ in DI water of 50 mL with stirring at 100 °C and 500 rpm. In an auxiliary beaker, $Na_3C_6H_5O_7$ of 0.5 g and 3 g of NaOH were mixed with 30 mL of DI water, stirring at room temperature and 500 rpm. The dropwise addition of the resulting solution into the $CuNO_3$ solution was performed while maintaining stirring at 100 °C for 10 min. Subsequently, the solution was subjected to centrifugation. Excess solvents have been disposed of down the sink, and the precipitates of copper

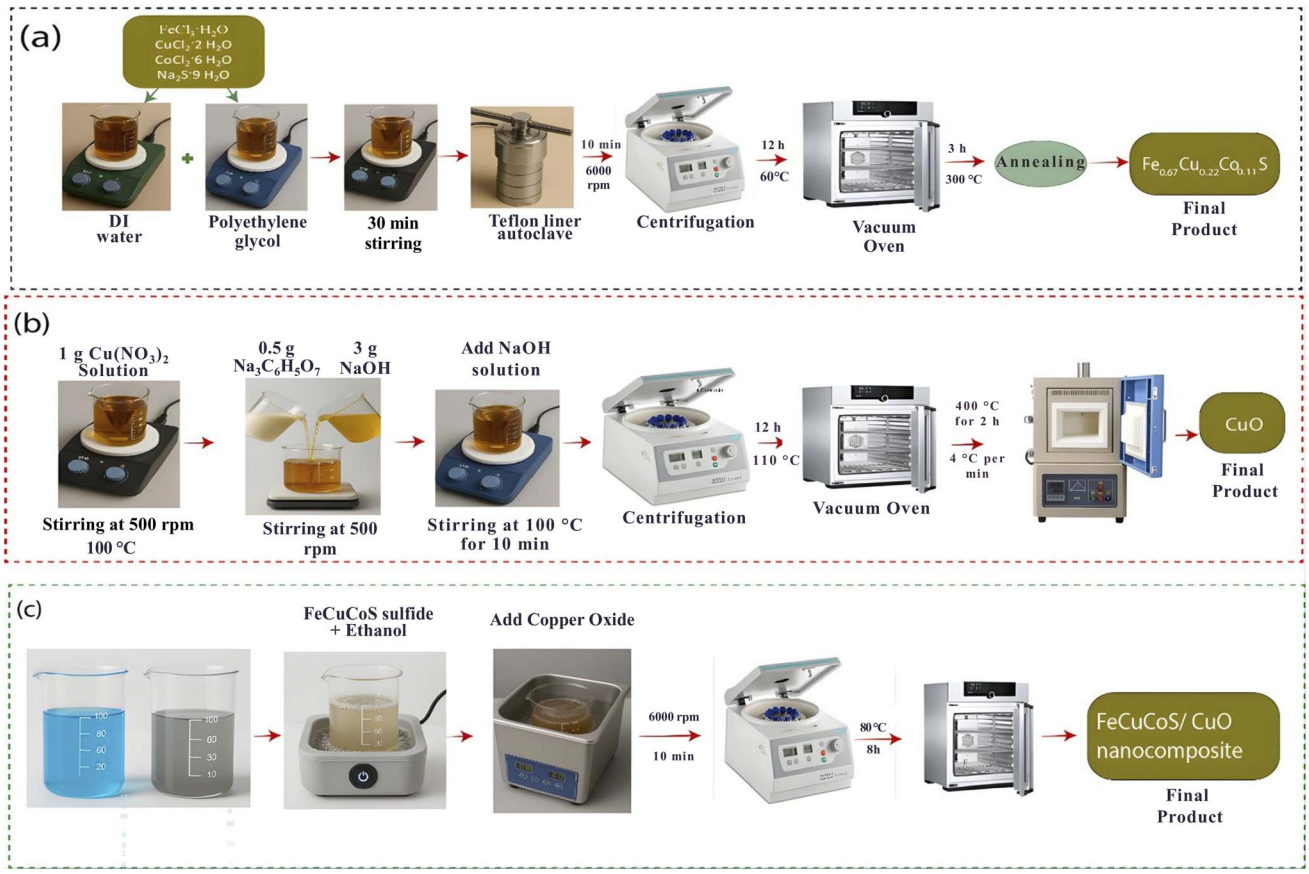

Fig. 1 Synthesis illustration of (a) $Fe_{0.67}Cu_{0.22}Co_{0.11}S$, (b) copper oxide, and (c) $Fe_{0.67}Cu_{0.22}Co_{0.11}S$/copper oxide nanocomposites.

citrate present in the centrifuge tubes were collected. The as-obtained powders were then dried at 110 °C for 12 h in an oven.

2.4 Conversion of copper citrate into copper oxide

Copper citrate is subjected to calcination under an air atmosphere at 400 °C for 2 hours at 4 °C per minute, which facilitates its thermal decomposition and subsequent formation of copper oxide, see Fig. 1(b). This process not only ensures the complete removal of organic constituents but also promotes the generation of copper oxide particles, also known as U2, with reduced dimensions, thereby enhancing surface area and potential reactivity.

2.5 Synthesis of $Fe_{0.67}Cu_{0.22}Co_{0.11}S$/copper oxide nanocomposite

The $Fe_{0.67}Cu_{0.22}Co_{0.11}S$/copper oxide synthesis began with the optimization of different ratios of transition metal sulfides and copper citrate. The first nanocomposite was prepared using a 3 : 1 ratio, where 75% (*i.e.*, 75 mg) sulfide particles in 30 mL of ethanol were put under probe sonication for 10 minutes, followed by the addition of 25% (*i.e.*, 25 mg) copper oxide. The resulting solution was then probe sonicated for another 10 minutes. To separate the precipitate from the solvent, a 10 minute centrifugation process was run at 6000 rpm. To obtain the final material, the precipitation was centrifuged under the same conditions and repeatedly rinsed with ethanol and DI water. After that, the ingredients were dried for 8 hours at 80 °C in an oven. Hence, the $Fe_{0.67}Cu_{0.22}Co_{0.11}S$/copper oxide nanocomposite was formed (abbreviated as U3), see Fig. 1(c). After optimization, another nanocomposite 4 : 1, 5 : 1, 6 : 1 ratio was also prepared, using the aforementioned synthesis to give $Fe_{0.67}Cu_{0.22}Co_{0.11}S$/copper citrate nanocomposites, abbreviated as U4, U5, and U6, respectively.

2.6 Preparation of the electrode

After synthesizing, U1 to U5 were prepared for slurries. For U1, 12 mg active material (that is, U1) and 1.5 mg of acetylene black were mixed and added to a slurry tube containing 30 μL PVDF and 40 μL NMP. The blend was stirred at 360 rpm for 8 hours. Nickel foam was used as a substrate for slurries to be deposited. The pre-cleaned nickel foam was washed with HCL, de-ionized water, acetone, and ethanol, each time placed under ultrasonication for 2–3 minutes in order to make sure that it is ready for slurry deposition. Then, the mixtures were uniformly drop-cast onto a Ni foam of 1 cm^2 area and dried at a temperature of 80 °C for a duration of 8 hours. Similarly, U2, U3, U4, U5, and U6 were also prepared with similar methods, but with modified compositions.

2.7 Asymmetric supercapacitor device fabrication

Activated carbon (AC) was employed internally as the negative electrode in production with U4 nanocomposite for the positive electrode, thereby configuring a supercapacitor device with a hybrid and asymmetric nature. The electrodes were joined using Teflon tape with a Hoffman filter paper as its separator and 1 M alkali KOH as an electrolyte. The preparation of the negative electrode involved mixing an active mass of AC, PVDF, and acetylene black in the ratios of 80, 10, and 10, respectively, inside NMP solvent. A micropipette was then used to apply this mixture onto a piece of porous Ni-foam (1 cm^2). The slurry-coated Ni-foam was placed in the vacuum oven, where it underwent drying for eight hours at 80 °C. Importantly, Table ST1 indicates the electrode mass ratios, active material loading, and charge balance parameters used for asymmetric supercapacitor device construction (Fig. 2).

2.8 Electrochemical analysis

The materials' electrochemical characterization was carried out following the guidelines using a three-electrode assembly of Gamry. A platinum disc as the counter electrode, an Hg/HgO reference electrode, and transition metal sulphides and copper citrate composites served as the system's working electrodes. The electrolyte utilized was a 1 M KOH solution in DI water. Electrochemical impedance spectroscopy (EIS), cyclic voltammetry (CV), and galvanostatic charge–discharge (GCD) techniques were employed to assess the charge/discharge behavior of the materials and their devices. The electrodes and the device's cyclic stability were tested using a potentiostat (Galvanostat, Reference 3000, Gamry Instruments, USA). Based on the cyclic voltammograms, the specific capacitance, C_s, of the corresponding electrode was calculated using the equation (eqn (1)).

$$C_s = \frac{\int_{v_i}^{v_f} I \times \Delta V}{m \times v \times \Delta V} \quad (1)$$

Here, v represents the potential scan rate in millivolts per second (mV s^{-1}), m the electrode material's mass in grams, ΔV the potential operating window, C_s the specific capacitance in farads per gram, and the integral function is the area under the CV curve. The specific capacity (Q_s) can be computed using the previously mentioned formula and the following sets of discharge curves.

$$Q_s = \frac{I \times \Delta t}{m} \quad (2)$$

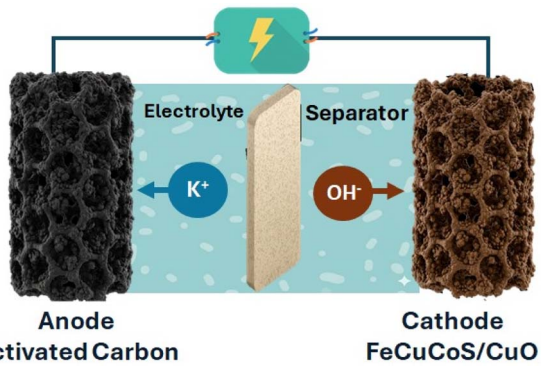

Fig. 2 Asymmetric supercapacitor device of $Fe_{0.67}Cu_{0.22}Co_{0.11}S$/CuO *vs.* activated carbon (AC).

where m is the mass of the electrode, Δt is the discharge time, and I represents the current and m represents the active mass of deposited material. Thus, this equation was used to calculate specific capacity from GCD curves using eqn (2).

$$C_s = \frac{I \times \Delta t}{m \times \Delta V} \quad (3)$$

where I is the current, Δt is the discharge time, m represents the active mass of deposited material, and ΔV is the potential operating window applied to determine specific capacitance from the GCD curve in eqn (3).[53]

The asymmetric supercapacitor device's energy density (E_d) in watt-hour per kilogram (Wh kg^{-1}) and power density (P_d) in watt per kilogram (W kg^{-1}) were calculated from eqn (4) and (5), respectively.

$$E_d = \frac{Q_s \times \Delta V}{3.6 \times 2} \quad (4)$$

where Q_s is the specific capacity, and ΔV is the potential operating window applied to determine energy density (E_d) in eqn (4).

$$P_d = \frac{3600 \times E_d}{\Delta t} \quad (5)$$

where E_d is the energy density calculated in eqn (4) and discharge time is denoted by Δt to determine power density (P_d) in eqn (5).

2.9 Characterization

Energy-dispersive X-ray spectroscopy (EDS), in conjunction with scanning electron microscopy (SEM, EVO 15, Carl Zeiss, Jena, Germany), was employed to examine the elemental composition and surface morphology of the as-synthesized $Fe_{0.67}Cu_{0.22}Co_{0.11}S$, copper oxide, and their U5 nanocomposite. Using an X-ray diffractometer (XRD, AXRD LPD, Proto, Ontario, Canada), the phase as well as structural characteristics were examined. Cu-Kα radiation ($\lambda = 1.5418$ nm) was used to record an X-ray intensity *versus* two-theta (2θ) pattern for the 2θ diffraction angle between 10° and 80°. For electrochemical analysis, a potentiostat (Galvanostat, Reference 3000, Gamry Instruments, Warminster, PA, USA) was used. A platinum (Pt) disc counter electrode and an Hg/HgO reference electrode were used in the three-electrode assembly setup for the electrode testing. As explained, Ni-foam was used to create the device and working electrode.

3 Results and discussion

3.1 Morphological, crystallographic, and spectroscopic analysis

As shown in Fig. 3(a1 and a2), the surface morphology of the as-prepared $Fe_{0.67}Cu_{0.22}Co_{0.11}S$ nanoparticles was studied by SEM, suggesting the irregularly shaped aggregated structure of $Fe_{0.67}Cu_{0.22}Co_{0.11}S$ nanoparticles. The wide range of particle sizes, agglomeration of nanoparticles, and large number of surfaces suggest good active sites for the electrochemical reactions. Such surface properties favor the mobility of electrons/ions, rendering the material an attractive candidate for electrochemical energy storage applications. The elemental area mapping (see Fig. 3(a4–a7)) of an area indicated in Fig. 3(a3) supports the homogeneous distribution of Fe, Cu, Co, and S, thereby demonstrating the successful synthesis of the ternary TMS. In contrast, the micrographs (Fig. 3(b1 and b2)) show the morphology of CuO samples with a very small-sized spherical texture, a characteristic of Cu-oxide-derived morphologies. Unlike $Fe_{0.67}Cu_{0.22}Co_{0.11}S$ nanoparticles, CuO nanoparticles showed higher agglomeration characteristics, which can be attributed to their relatively higher surface energy. This specific morphology forms a unique structural network that can affect electrochemical performance by modulating electron mobility and surface availability. The elemental area maps of CuO nanoparticles of an area indicated in Fig. 3(b3), see Fig. 3(b4 and b5), which shows the presence of evenly distributed Cu and O, which is an indication of citrate-derived copper oxide. On the other hand, Fig. 3(c1 and c2) depicts the morphology of the material of interest, nanocomposites, *i.e.*, $Fe_{0.67}Cu_{0.22}Co_{0.11}S$/CuO (weight percentage ratio of 5 : 1), indicating a more complex surface. The nanocomposites display large agglomeration, providing a porous structure with smaller nanoparticles of CuO composited with the larger $Fe_{0.67}Cu_{0.22}Co_{0.11}S$ nanoparticles. This linked architecture enhances surface area and charge-transfer kinetics. The elemental area maps of an area indicated in Fig. 3(c3), see Fig. 3(c4–c8), indicate a uniform dispersion of Fe, Cu, Co, S, and O, thus confirming the successful compositing of $Fe_{0.67}Cu_{0.22}Co_{0.11}S$ with CuO.[54,55] In SI, see Fig. S1, the elemental analysis of the synthesized materials is corroborated by the EDS spectra. In the spectrum Fig. S1(a), $Fe_{0.67}Cu_{0.22}Co_{0.11}S$ produced strong peaks due to the elements Fe, Cu, Co, and S, suggesting that all four elements were present effectively. Similarly, the spectrum Fig. S1(b) of CuO showed characteristic peaks of Cu and O corresponding to its elemental composition. In the spectrum Fig. S1(c), the $Fe_{0.67}Cu_{0.22}Co_{0.11}S$/CuO composition exhibited the required characteristic peaks of Fe, Cu, Co, S, and O, implying the successful composite formation of $Fe_{0.67}Cu_{0.22}Co_{0.11}S$ and CuO.

The XRD patterns of the synthesized nanomaterials and nanocomposites, as shown in Fig. 4(a), revealed distinct crystalline features for $Fe_{0.67}Cu_{0.22}Co_{0.11}S$, CuO, and $Fe_{0.67}Cu_{0.22}Co_{0.11}S$/CuO nanocomposites. The $Fe_{0.67}Cu_{0.22}Co_{0.11}S$ nanoparticles sample exhibited well-defined peaks at 2θ values of 29.5°, 34.2°, and 58.5°, which are indexed to the (111), (200), and (311) according to JCPDS card number 01-075-0253 (ref. 52) and 46.9°, indexed to (200) according to JCPDS card number 03-1050 (ref. 56) to the $Fe_{0.67}Cu_{0.22}Co_{0.11}S$ phase's planes, confirming the formation of a stable multimetallic sulfide structure. Similarly, the CuO nanoparticles sample showed characteristic peaks at 2θ angles of 32.5°, 35.56°, 38.71°, 48.99°, 53.63°, 58.43°, 61.59°, 66.01°, 68.21°, 72.59°, and 75.60°, corresponding to the (110), (−111), (111), (−202), (020), (202), (113), (311), (221), (311), and (−222) planes, respectively, according to JCPDS card number 01-080-0076,[57] which are consistent with the crystalline structure of copper oxide. The composite $Fe_{0.67}Cu_{0.22}Co_{0.11}S$/CuO displayed diffraction peaks at 2θ angles of 29.5°, 34.2°, 38.71°, 46.9°, and 58.5°, indexed to the (111), (200), (111), (200), and (311) planes of

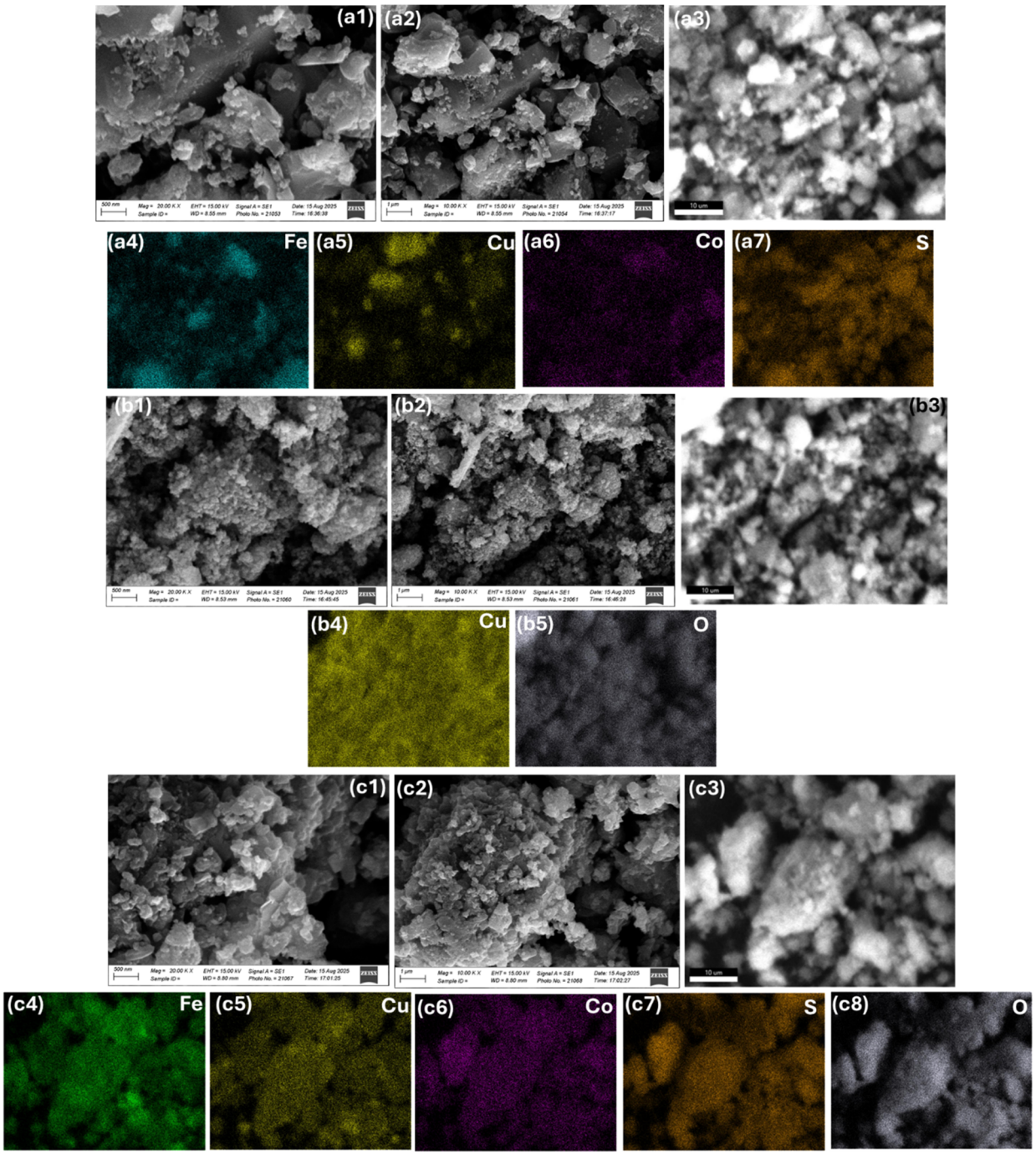

Fig. 3 SEM images at various magnifications and elemental area maps of (a1–a7) $Fe_{0.67}Cu_{0.22}Co_{0.11}S$, (b1–b5) CuO, (c1–c8) $Fe_{0.67}Cu_{0.22}Co_{0.11}S$/CuO (U5).

$Fe_{0.67}Cu_{0.22}Co_{0.11}S$ and CuO. It is worth noting that peaks shift at low and higher angles, which is consistent with the other reported literature and basic understanding of nanocomposites. Moreover, these results suggest that the nanocomposite material successfully integrates the CuO phase into the $Fe_{0.67}Cu_{0.22}Co_{0.11}S$ matrix while maintaining its crystalline framework.

Moreover, in order to examine the functional groups of pristine and nanocomposite samples, *i.e.*, $Fe_{0.67}Cu_{0.22}Co_{0.11}S$, CuO, and $Fe_{0.67}Cu_{0.22}Co_{0.11}S$/CuO nanocomposites, FTIR analysis was conducted within the wave number range of 500–4000 cm^{-1}, see Fig. 4(b). The FTIR spectrum of $Fe_{0.67}Cu_{0.22}Co_{0.11}S$ exhibited a broad band at 3009 cm^{-1}, attributed to O–H stretching vibrations from surface hydroxyl groups and adsorbed water molecules. In contrast, the band at 1740 cm^{-1} corresponds to C=O stretching vibrations, likely originating from surface carbonyl groups or residual organic species.[58] A distinct band at 1050 cm^{-1} is assigned to C–O stretching modes

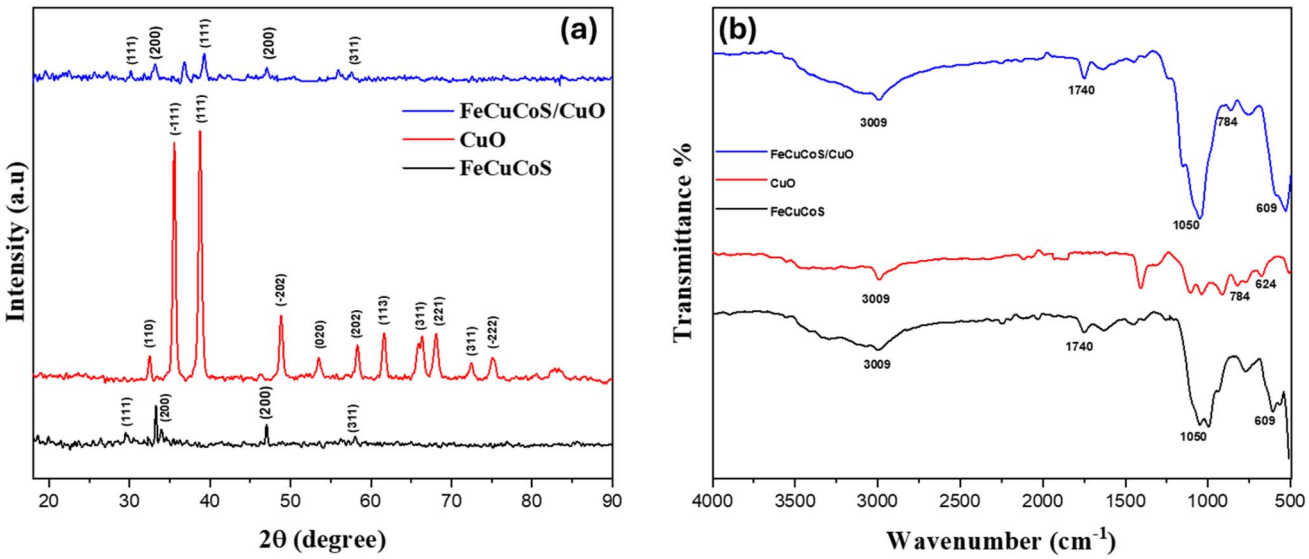

Fig. 4 (a) XRD patterns (b) FT-IR spectra of $Fe_{0.67}Cu_{0.22}Co_{0.11}S$, CuO, and $Fe_{0.67}Cu_{0.22}Co_{0.11}S$/CuO.

coupled with metal–oxygen vibrations,[59] and the strong absorption at 609 cm^{-1} corresponds to Fe–S/Co–S stretching, confirming the presence of transition metal sulfide bonds.[60] In the case of CuO, the bands at 624 cm^{-1} and 784 cm^{-1} are characteristic of Cu–O stretching vibrations,[61] while the O–H stretching at 3009 cm^{-1} further supports hydroxyl group adsorption.[62] For the $Fe_{0.67}Cu_{0.22}Co_{0.11}S$/CuO composite, all characteristic peaks of both sulfide and oxide phases are present: the O–H stretching at 3009 cm^{-1}, C=O stretching at 1749 cm^{-1}, C–O stretching at 1050 cm^{-1}, polysulfide vibrations at 609 cm^{-1}, and Cu–O stretching at 784 cm^{-1}, indicating the coexistence of both structural units. The simultaneous presence of these distinct vibrational features confirms the successful incorporation of CuO into the $Fe_{0.67}Cu_{0.22}Co_{0.11}S$ matrix.

3.2 Electrochemical analysis of a three-electrode assembly

Cyclic voltammetry (CV) helps confirm the electrochemical behavior by measuring intrinsic electrochemical properties over a potential range of 0–0.7 V. The CV curves obtained in a three-electrode setup with a 1 M KOH electrolyte were analyzed over scan rates from 3 to 50 mV s^{-1}. The analysis considers scanning speeds ranging from 3 to 50 mV s^{-1}, as shown in Fig. 5.

With an increase in scan rate from 3 mV s^{-1} to 50 mV s^{-1}, all samples show that their oxidation peak shifts towards higher potentials, which can be attributed to a lag in the diffusion of electroactive species, and the fast alteration of potential, creating a higher charge-transfer resistance that requires greater energy for oxidation to occur. Moreover, the reference sample, U1, *i.e.*, $Fe_{0.67}Cu_{0.22}Co_{0.11}S$, exhibited unique redox peaks in its cyclic voltammogram. Fig. 5(a) shows how the CV curves of U1 appear at different scan rates, showing narrow oxidation and broader reduction curves. Similarly, the CV profiles of pristine CuO (abbreviated as U2), at various scan rates, see Fig. 5(b), indicate its battery-grade behavior: with an increase in current response proportional to the rise in scan rate from 3 to 50 mV s^{-1}, indicating good rate capability. This indicates they have a faradaic charge storage mechanism, typical characteristics of battery-type electrode materials. These faradaic redox peaks further arise from reversible redox actions between electrolytic ions and active electrode materials. This was reflected by anodic and cathodic currents present in each scan. However, it must be noted that the maximum oxidation current of U1 is higher than that of U2, indicating CuO can only enhance the performance of U1 by creating optimal conductive channels and mesoporosity.

Furthermore, the reference sample U3, *i.e.*, $Fe_{0.67}Cu_{0.22}Co_{0.11}S$/CuO (having a 3 : 1 weight percentage ratio) nanocomposites, exhibited a cyclic voltammogram with unique redox peaks. Fig. 5(c) shows how the CV curves of U3 appear at different scan rates, showing oxidation and reduction peaks, evidently proving the faradaic reactions to take place upon the application of voltage. The area enclosed by the CV curves for U3 is reduced in comparison to U1, indicating non-optimal conductive channels formation; thus, it decreases the charge storage capacity. Similarly, the CV curves of U4, U5, and U6, having 4 : 1, 5 : 1, and 6 : 1 weight percentage ratios, see Fig. 5(d–f), exhibit a distinct pair of broad, symmetric faradaic redox peaks.[63] Among all nanocomposite electrode materials, the change in peak intensity and shape is due to different $Fe_{0.67}Cu_{0.22}Co_{0.11}S$: CuO ratios (4 : 1, 5 : 1, and 6 : 1), which affect the active surface area and electronic conductivity of the electrode material. In addition, U5 stood the best and material of interest since it achieved the highest area under the CV curves and the largest oxidation peak currents, clearly suggesting its highest capability to store relatively maximum energy in comparison with other electrode materials.

Galvanometric charge–discharge (GCD), see Fig. 6(a–f), was studied for various electrode materials, *i.e.*, U1–U6, at 0.7–6 A g^{-1} within the potential window of 0–0.5 V. They show non-linear charge–discharge profiles for all the electrodes tested, indicating the faradaic redox reactions other than pure electrostatic double-layer storage.[52,64] As a result, the total discharge

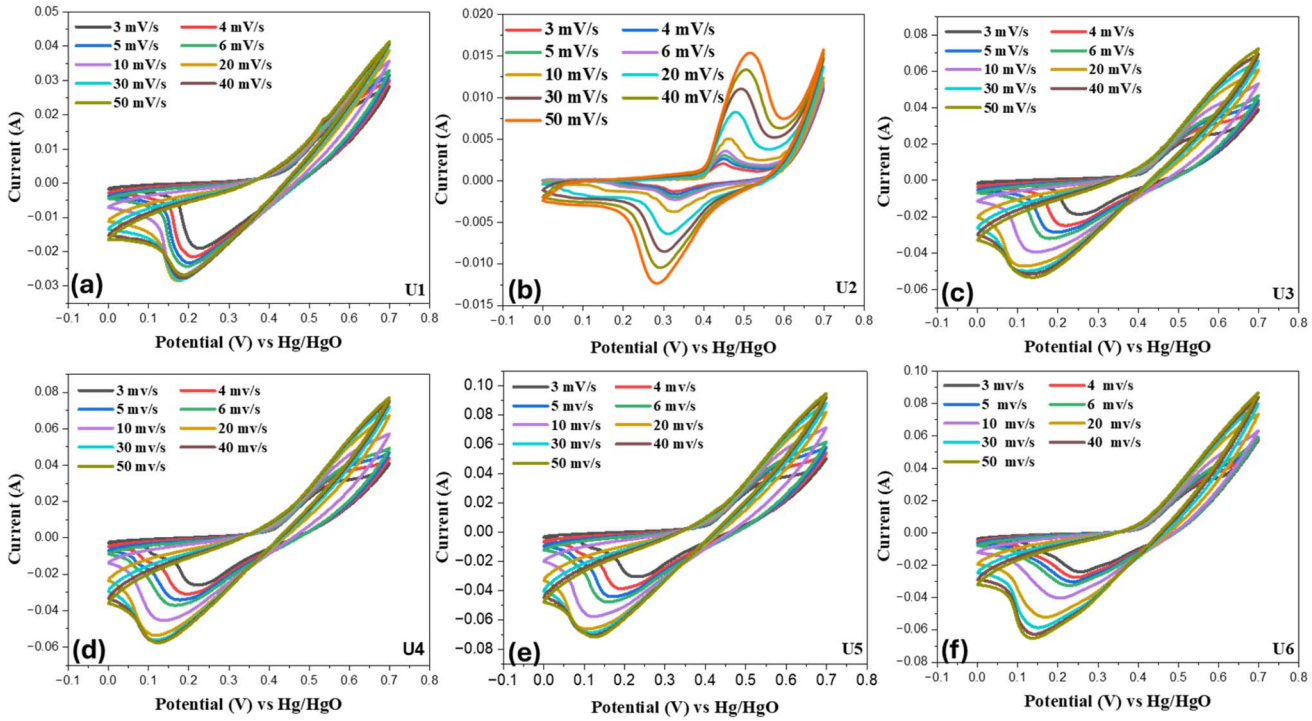

Fig. 5 Cyclic voltammetry of the five electrodes, *i.e.*, (a) U1, (b) U2, (c) U3, (d) U4, (e) U5, and (f) U6, recorded at different scan rates using a three-electrode assembly.

time of U1, U2, U3, U4, U5, and U6 were 256.3 s, 8.4 s, 635.1 s, 857.4 s, 1005 s, 480.5 s, respectively. This clearly indicates that U5 outperforms other electrode materials. The final consistency observed in GCD profiles was also scaled among the current densities, confirming even further the high reversibility and good electrochemical stability of these electrodes. In other words, these results show that these electrodes are possible candidates from the viewpoint of efficient redox activity for

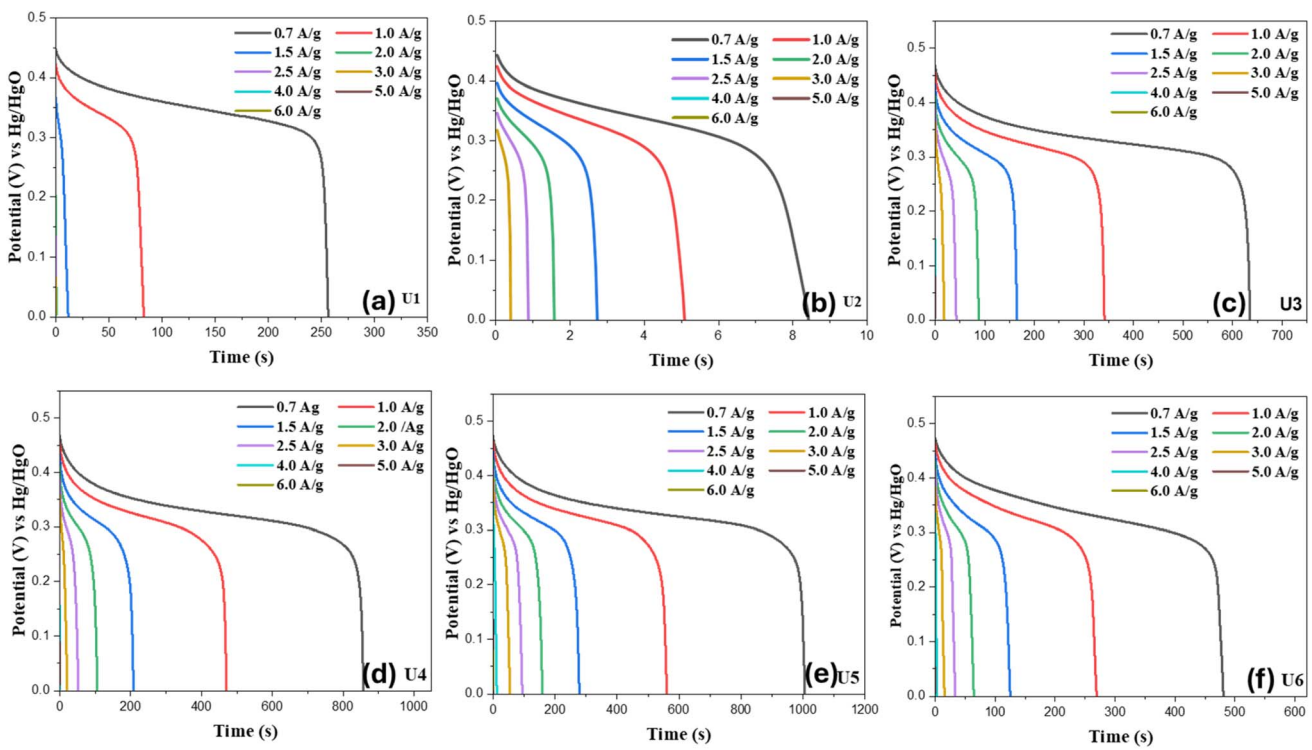

Fig. 6 GCD curves for various electrodes at 0.7–6 A g^{-1}, *i.e.*, (a) U1, (b) U2, (c) U3, (d) U4, (e) U5, and (f) U6.

battery-type behavior, as shown in Fig. S2, suitable for high-performance energy storage applications.

3.2.1 Comparative analysis of various electrodes. The comparison of CV curves of various electrodes, see Fig. 7(a), reveals that all electrodes, except for U2 (CuO), exhibit quasi-rectangular shapes with distinct redox features, confirming the contributions of an EDLC pseudocapacitive mechanism, *i.e.*, hybrid behavior. Among the samples, U5 shows the largest enclosed areas, indicating higher charge storage capability. In contrast, pristine CuO displays the lowest current response and smallest integrated area, reflecting poor electrochemical activity. The GCD profiles, see Fig. 7(b), further confirm these trends. All electrodes demonstrate nearly symmetric charge–discharge patterns, signifying good reversibility of the electrochemical process. The discharge times are significantly longer for U5, corresponding to their higher specific capacitance values, while U1 and U2 exhibit much shorter discharge durations, confirming their relatively weak charge storage ability. EIS was performed in a three-electrode cell setup with a frequency range of 1–100 000 Hz to evaluate the electrode–electrolyte interfacial resistance, as well as the charge-transfer mechanism. Fig. 7(c) displays the Nyquist plot of U1–U5 samples, with an inset demonstrating the spectra of the high-frequency region. The series resistance (R_s) was represented by the X-intercept in the high-frequency region of the EIS plot, as shown in the inset, and it contains the electrode resistances, electrode–electrolyte interface resistance, and electrolyte resistances. The R_s values in U1–U6 were found to be 6.2 μΩ, 7.7 μΩ, 1.2 μΩ, 32 μΩ, 0.62 μΩ, and 2.05 Ω respectively, exhibiting a smaller R_s value in U5. Also, U5 exhibits a smaller semicircle behavior, implying lower charge-transfer resistance (R_{ct}) in the high-frequency region. Additionally, in the low frequency region, the W_d is represented by a vertical straight line, which arises from OH^- ion diffusion in the electrolyte. U5 shows a lower W_d value, as it aligns more vertically with the *Y*-axis compared to the other electrodes. In the low-frequency region, the rate of diffusion of electrolyte ions within the electrode material is also inversely proportional to the length of the EIS spectrum line. The ability to transfer the OH ions more rapidly within the U5 electrode material is explained by a shorter ion diffusion path. This confirms that U5 exhibits superior electrochemical performance, as demonstrated by its higher electrical conductivity. The results of EIS measurements align well with those from CV and GCD, indicating that the U5 electrode material achieves optimized electrochemical performance in the three-electrode setup.

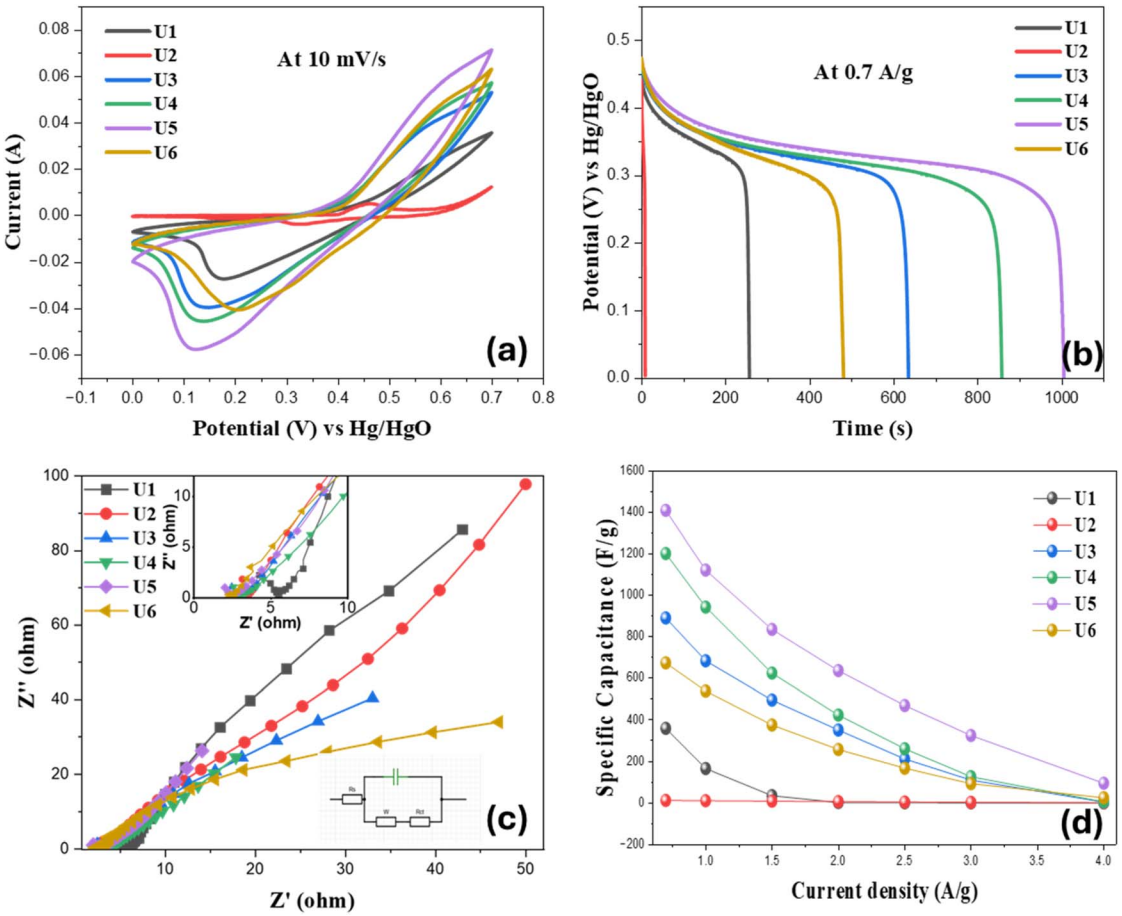

Fig. 7 (a) CV comparison at 10 mV s^{-1} scan rates, (b) GCD comparison at 0.7 A g^{-1}, (c) Nyquist plots comparison, (d) specific capacitance at various current densities for U1–U6.

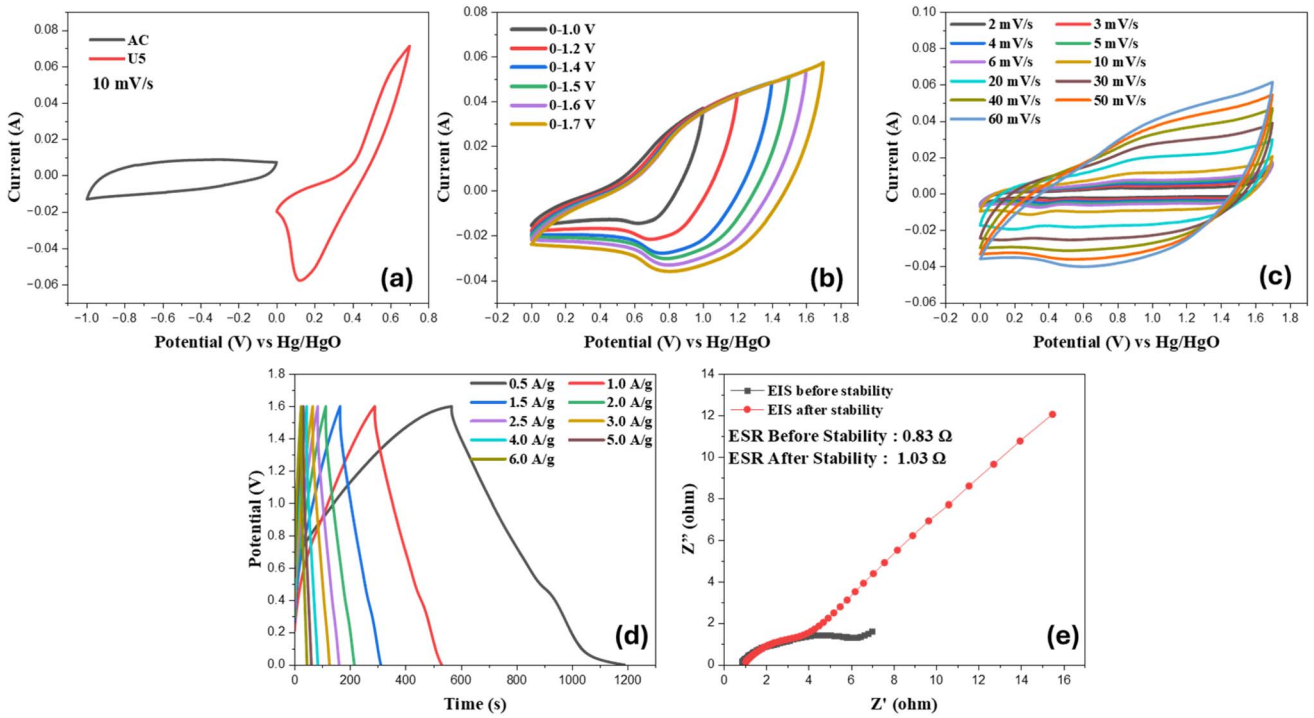

Fig. 8 (a) Three-electrode assembly tested CV of activated carbon and U5 at 10 mV s^{-1} scan rate, (b) optimal potential window graph of U5 for finding optimal potential window, (c) CV of device from 2 mV s^{-1} to 60 mV s^{-1} scan rates, (d) GCD of U5||AC asymmetric supercapacitor device from 0.5 A g^{-1} to 8.0 A g^{-1}, and (e) Nyquist plot comparison of U5||AC before and after stability testing.

The specific capacitance for each electrode was calculated using eqn (2) and (3), and GCD curves at different current densities. Fig. 7(d) shows that for all samples, the specific capacitance value showed an inverse relation with current densities, which can be ascribed to the insufficient time available for the ions to reach the active sites of electrode materials. As a result, U1, U2, U3, U4, U5, and U6 indicated specific capacitances of 358.82 F g^{-1}, 11.7 F g^{-1}, 889.14 F g^{-1}, 1200.36 F g^{-1}, 1407 F g^{-1}, and 672.7 F g^{-1}, respectively, at the 0.7 A g^{-1} current densities. The graph indicates that pristine U1, *i.e.*, $Fe_{0.67}Cu_{0.22}Co_{0.11}S$ electrode material, shows a bit higher specific capacitance than U2 (*i.e.*, CuO); however, it is still inferior to any of its nanocomposite electrode materials (*i.e.*, U3–U6), clearly suggesting the nanocomposites potentially possess much better prospects in advanced energy storage and battery-related applications.[54] In addition, as U2 shows a minimal specific capacitance compared to U1, the higher specific capacitance of U3–U6 signifies that it can predominantly be attributed to the conducting channels and optimal mesoporosity introduced due to the composite formation by combining U1 and U2 in different ratios. More importantly, it indicates that U5 outperforms pristine as well as all other nanocomposite electrodes by showing the comparatively highest specific capacitance value of 1407 F g^{-1}. This points to an ideal composite formation that facilitates excellent charge storage and fast redox kinetics. Moreover, interestingly, U5 showed excellent capacitance retention even at higher current densities, ensuring that it remains superior in terms of rate performance compared to other compositions.

3.3 Electrochemical analysis of the asymmetric supercapacitor device

According to the literature, the best-performing electrode in a three-electrode assembly is chosen for further electrochemical analysis in a two-electrode assembly to devise its practical applicability in real-time applications. For this, herein we analyzed our best-performing electrode materials, *i.e.*, U5, in a two-electrode assembly using its asymmetric supercapacitor device. It was comprised of U5 as the positive electrode, activated carbon (AC) as the negative electrode, alpha-cellulose as the separator, and 1 M KOH solution in DI water as the electrolyte. Based on previous studies, the AC electrode and the best performing electrode material (U5), as shown in Fig. 8(a), are analyzed in three electrode assemblies in order to show their behavior, *i.e.*, EDLC/pseudo/hybrid/battery-grade. Fig. 8(a) shows a characteristic rectangular-looking CV curve within 0 to −1.0 V, typical of EDLC behavior, while the U5 electrode exhibited notable redox peaks in the range of 0–0.7 V, characteristic of faradaic-type behavior. Electrode mass ratios, active material loading, and charge balance calculations and their results are shown in the table. ST1 is used for asymmetric supercapacitor device construction to ensure reliable and reproducible device electrochemical performance.[65] U5, as shown in Fig. 8(b), was observed to display enhanced potential windows of 0–1.7 V with quasi-rectangular and redox characteristics, thus confirming the hybrid nature of the supercapacitor. Furthermore, CVs at scan rates of 2–60 mV s^{-1}, see Fig. 8(c), retained their shape even at higher scan rates, highlighting the good reversibility, rate capability, and

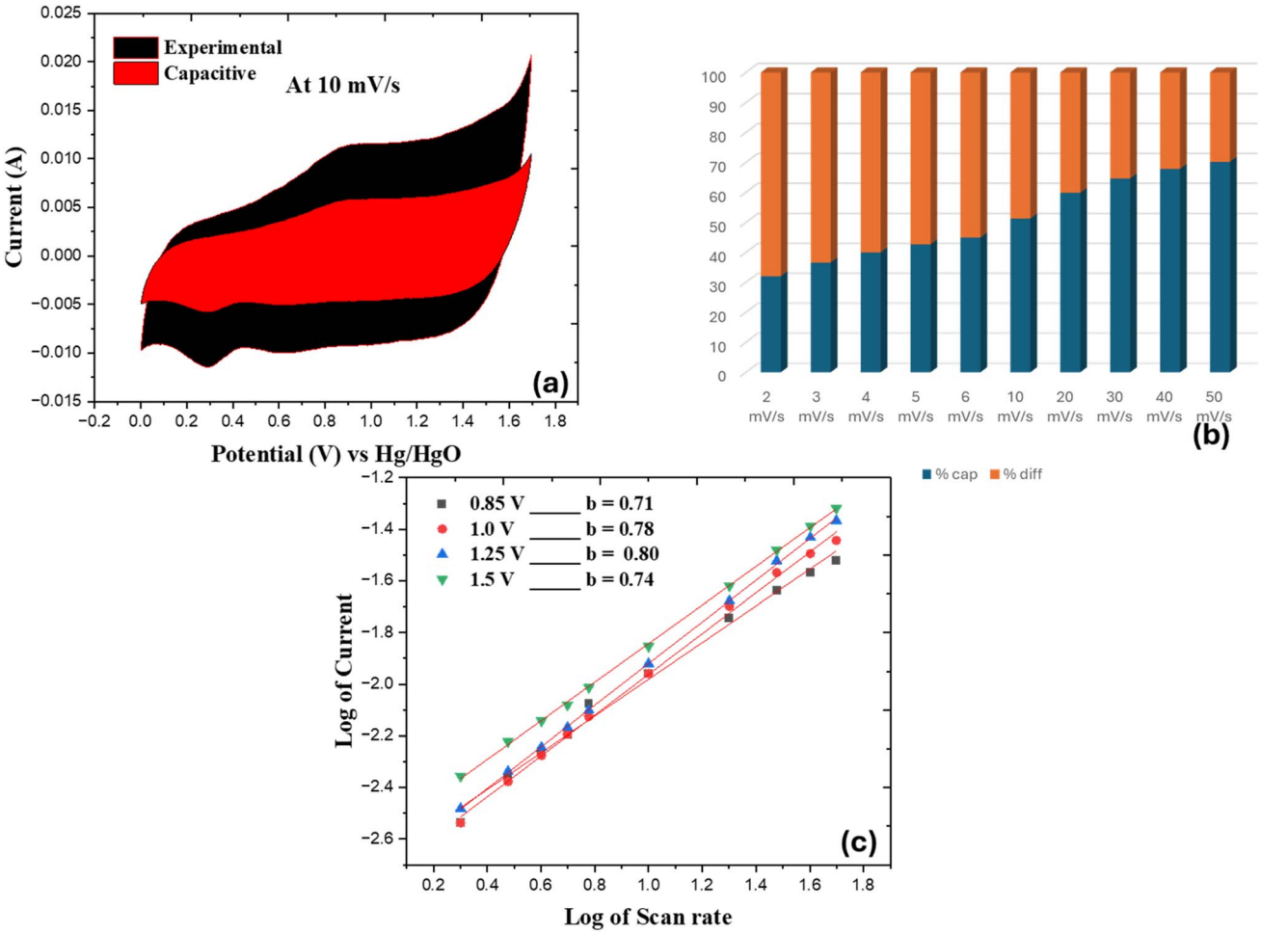

Fig. 9 (a) Semiempirical approach to separate the capacitive controlled region from experimental data at 10 mV s^{-1}, (b) bar chart showing capacitive and diffusive percentage contribution at several scan rates (2–50 mV s^{-1}), and (c) *b*-values for showing the behavior of the supercapacitor device.

electrochemical stability of the device. The GCD profiles of their asymmetric supercapacitor device, *i.e.*, U5||AC, presented in Fig. 8(d), were evaluated at varied current densities (0.5–6 A g^{-1}) over the operating voltage window of 0–1.6 V. The discharge curves are, however, slightly non-linear, suggesting the coexistence of capacitive and faradaic storage mechanisms. Using eqn (2) and the maximum discharge time at 0.5 A g^{-1} in Fig. 8(d), a very high specific capacity of 311 C g^{-1} was delivered by the asymmetric supercapacitor device. Nevertheless, with increasing current density, there was a gradual decrease in the discharge time, which is typical for hybrid supercapattery systems and might be because of the insufficient availability of time for the ions to reach the active sites of electrode materials. The electrochemical impedance spectroscopy (EIS) was further conducted before and after the cycling stability for 3000 cycles, and their Nyquist plots are represented in Fig. 8(e). The device showed low series resistance (R_s) before stability, *i.e.*, 0.83 Ω, and a slightly increased value of 1.03 Ω even after prolonged 3000 charge–discharge cycles, showing a minimal increase in internal resistance and slightly decreased capacitance retention prospect (see Fig. 10(c)). The high-frequency region semicircle represents charge-transfer resistance, while the straight line in the low-frequency region reveals excellent ion diffusion capability. These results further confirm that the device on U5||AC is an electrochemically reliable, low internal resistance, and highly potential candidate for next-generation energy storage devices.

3.3.1 Capacitive and diffusive nature analysis. Furthermore, the semiempirical (Dunn's model) approach was employed to further scrutinize the hybrid SC performance. The asymmetric device (U5||AC) consists of both diffusive and capacitive electrodes, which exhibit faradaic (reversible redox) and non-faradaic (ionic adsorption and desorption) phenomena. The cumulative current $i_{(v)}$ achieved from the real device is the combination of both diffusive $i_{(F)}$ (Faradaic reactions) and capacitive $i_{(nF)}$ (non-Faradic reactions); therefore,

$$i_{(v)} = i_{(F)} + i_{(nF)} \quad (6)$$

Capacitive contributions result from non-Faradic reactions; therefore,

$$i_{(nF)} = K_1 v \quad (7)$$

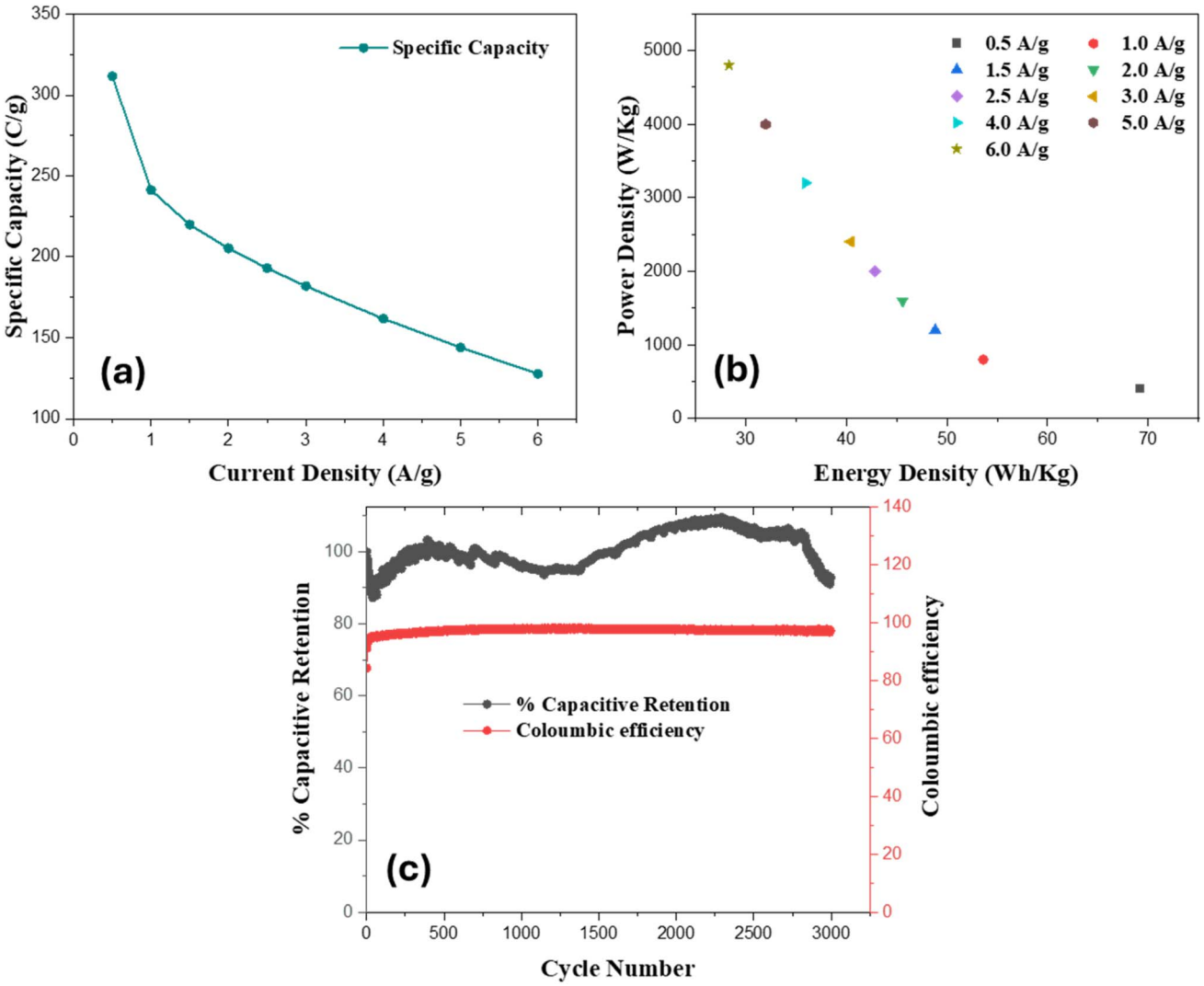

Fig. 10 Asymmetric supercapacitor device's (U5||AC) (a) specific capacity graph at various current densities, (b) Ragone plot showing power density against energy density at various current densities, and (c) stability and coulombic efficiency till 3000 cycles.

where k_1 is the arbitrary constant and v is the sweep rate (mV s^{-1}). Faradaic reactions $i_{(nF)}$ reveal both diffusion (contribution obtained from inside bulk reactions ($i_{(b)}$)) as well as capacitive-controlled reaction from the surface ($i_{(s)}$), *i.e.*,

$$i_{(F)} = i_{(s)} + i_{(b)} \quad (8)$$

$$i_{(F)} = i_{(s)} + i_{(b)} = K_a v + K_b v^{1/2} \quad (9)$$

where $i_{(b)}$ mimics the diffusive contribution ($K_2 v^{1/2}$) and reflects the capacitive part $K_1 v$. By substituting eqn (7) and (9), eqn (6) will be,

$$i_{(v)} = K_1 v + K_a v + K_b v^{1/2} \quad (10)$$

By uniting the capacitive terms ($K_1 + K_a = K_c$), we obtain:

$$i_{(v)} = K_c v + K_b v^{1/2} \quad (11)$$

Dividing both sides by $v^{1/2}$ eqn (11) yields:

$$\frac{i_{(v)}}{v^{1/2}} = K_c v^{1/2} + K_b \quad (12)$$

Eqn (12), slope-intercept form, is particularly important because by plotting $i_{(v)}/v^{1/2}$ against $v^{1/2}$, the K_c (slope) reveals the capacitive (non-faradic/EDLC) behavior percentage, while its K_b (intercept) indicates the diffusive (faradaic/pseudocapacitive) behavior percentage.[66] A similar method was used to identify the capacitive and diffusion contributions of the U5||AC hybrid supercapacitor device; see Fig. 9(a). The analysis shows a 51.31% capacitive-contribution and 48.68% diffusive-contribution at 10 mV s^{-1}, indicating capacitive-dominant behavior of the supercapacitor device. The experimental CV curve $i_{(v)} = K_c v + K_b v^{1/2}$ is represented by the black-shaded region, while the capacitive-controlled contribution $i_{(nF)} = K_1 v$ is depicted by the red-shaded region inside the CV curve. Fig. 9(b) illustrates a bar chart at various scan rates showing the percentage contribution of diffusive and capacitive-controlled reactions in the entire device. The capacitive contribution

Table 1 Contrast between the reported literature and the present work, signifying its clear merit over others

Electrode materials	Synthesis method	Morphology/shape	E_d (Wh kg^{-1})|P_d (W kg^{-1})	Capacitance retention (%)|cycles	Ref.
$NiCo_2O_4$@$NiCo_2S_4$ core–shell (hybrid)	Hydrothermal + sulfidation	Core-shell nanowire/nanotube arrays	35.6|1500 at 2 A g^{-1}	~70.5% retention (reported under device cycling)	67
$NiCo_2S_4$ nanosheets/graphene	Hydrothermal + annealing	Nanosheets	35.1|1472.9	85% over 5000 cycles	68
$NiCo_2S_4$@PPy	Hydrothermal ($NiCo_2S_4$) + *in situ* PPy polymerization	Dandelion-like microspheres on Ni foam	35.17 Wh kg^{-1} 1472.29 W kg^{-1}	85% after 1500 cycles	63
ZIF-derived $NiCo_2S_4$	Sulfidation	Hollow cubic	~33|800 at 5 A g^{-1}	~67% after 10 000 cycles	69
CuS–graphene oxide	Hydrothermal + reduction	Nanoparticles	6.2|5300 at 5 A g^{-1}	~70% after 5000 cycles	70
$Fe_{0.67}Cu_{0.22}Co_{0.11}S$/CuO	Sonication-assisted solvothermal	Aggregated nanoparticles, partially porous	70|100 at 5 A g^{-1} 28|4800 at 6 A g^{-1}	~90% after 3000 GCD cycles	This work

increased with the rise in voltage sweep rate because there was insufficient time for the charges to diffuse into the active material. At 10 mV s^{-1}, the U5‖AC supercapacitor device showed a capacitive contribution of 51.31%, which increases to 70.21% at a scan rate of 50 mV s^{-1}.

To further validate the nature of the supercapacitor device, power-law fitting yielded *b*-values that are usually calculated. The *b*-value fitting was performed at several voltages between 0.85 and 1.5 V to determine the potential-dependent kinetics of the asymmetric hybrid device. Since capacitive-controlled and diffusive-controlled contributions vary with applied voltage, *b*-value fitting was used at several voltages to provide a more reliable charge-storage mechanism rather than a single potential. It is worth noting that if the value of *b* is approximately equivalent to 0.5, the device is considered as purely a battery-type supercapacitor device; if its value is 1, it signifies the pure capacitive-type supercapacitor device; if its value is intermediate and ranges from 0.5 to 0.8, it is considered as a hybrid-type supercapacitor device. Furthermore, the *b*-value fitting at several voltages between 0.85 and 1.5 V is presented in Fig. 9(c). The calculated *b*-value of our device ranges from 0.71 to 0.80, revealing a hybrid supercapacitor device. Additionally, the *b*-values obtained for U5‖AC support our claim that it is a hybrid-type of supercapacitor device.

3.3.2 Ragone plot and stability analysis. As depicted in Fig. 10(a), the device displayed a substantially higher specific capacity of ~311 C g^{-1} at a current density of 0.5 A g^{-1}. While at 6 A g^{-1}, it outstandingly maintained ~127 C g^{-1}, confirming good rate capability. The power as well as energy densities were then fully evaluated, and a Ragone plot, as shown in Fig. 10(b), was plotted. The fabricated device showed excellent performance with an energy density of ~70 Wh kg^{-1} and a power density of ~800 W kg^{-1} at 0.5 A g^{-1}. Notably, it maintained an energy density of ~28 Wh kg^{-1} even at a higher current density, *i.e.*, 6 A g^{-1}, while sustaining an incredible power density of ~4800 W kg^{-1}. Fig. 10(c) demonstrates the long-term cycling performance of the device, putting on display a steady capacitive retention of ~92.86% coupled with almost constant coulombic efficiency of 97.1% after 3000 GCD cycles, revealing highly reversible charge–discharge processes, negligible side reactions, excellent stability, and energy utilization. Hence, these results validate the remarkable durability, reversibility, and field application potentials of the fabricated electrode material.

3.3.3 Comparison with literature. Table 1 highlights a comparative analysis of various reported electrode materials, clearly demonstrating the competitive performance of U5 (*i.e.*, $Fe_{0.67}Cu_{0.22}Co_{0.11}S$/CuO, having a 5 : 1 weight percentage ratio, respectively). Unlike conventional $NiCo_2O_4$, $NiCo_2S_4$, and CuS-based electrodes, which often suffer from moderate energy densities (≈30–36 Wh kg^{-1}) or poor long-term stability, $Fe_{0.67}Cu_{0.22}Co_{0.11}S$/CuO electrode delivers a remarkably high energy density of 70 Wh kg^{-1} at a power density of 100 W kg^{-1}, and still sustains 28 Wh kg^{-1} even at a much higher power density of 4800 W kg^{-1}. Moreover, the electrode exhibits excellent durability, retaining ~92.86% of its capacitance over 3000 GCD cycles, which surpasses or matches the stability of

many previously reported systems. These results underline the superior electrochemical reversibility and robustness of our synthesized material. Therefore, the $Fe_{0.67}Cu_{0.22}Co_{0.11}S$/CuO electrode stands out as an efficient and durable candidate for advanced supercapattery applications, offering an advantageous balance between energy density, power density, and cycling stability compared to existing literature reports.

Supercapacitors, considered a potential energy storage device, can address the long-awaited problem of the energy crisis by storing energy for efficient, rapid, and sustainable utilization across diverse applications ranging from portable electronics to large-scale power systems. Herein, we have prepared a novel nanocomposite material *via* a novel ultrasonication-assisted solvothermal approach, combining the nanoparticles of $Fe_{0.67}Cu_{0.22}Co_{0.11}S$ and CuO in different weight percentage ratios. X-ray diffraction, scanning electron microscopy, and Fourier transform infrared spectroscopy analyses confirmed the successful synthesis of the targeted nanocomposites. Electrochemical evaluation revealed that the 5 : 1 composition (denoted as U5), identified as optimal material, exhibited a remarkable specific capacitance of 1407 F g^{-1} at 0.7 A g^{-1}, corresponding to enhancements of 3.9-fold and 120-fold compared to pristine $Fe_{0.67}Cu_{0.22}Co_{0.11}S$ and CuO, respectively. Furthermore, the asymmetric supercapacitor device based on U5 demonstrated superior electrochemical performance, delivering a specific capacity of 311 C g^{-1} at 0.5 A g^{-1}, an energy density of 70 Wh kg^{-1}, a power density of 4800 W kg^{-1}, a coulombic efficiency of 97.1%, and a long-term cycling stability of 92.86% after 3000 cycles. Dunn's model analysis indicated that charge storage was predominantly capacitive (51.3% at 10 mV s^{-1}), while power-law fitting yielded *b*-values between 0.71 and 0.80, signifying hybrid supercapacitor behavior. These results underscore $Fe_{0.67}Cu_{0.22}Co_{0.11}S$/CuO nanocomposites' potential as durable and high-performance materials for advanced energy storage applications.

4 Conclusion

Novel nanocomposites, combining the nanoparticles of $Fe_{0.67}Cu_{0.22}Co_{0.11}S$ and CuO in different weight percentage ratios, were synthesized using an ultrasonication-assisted solvothermal approach. The XRD, SEM, and FTIR results confirmed the successful preparation of pristine as well as nanocomposites. Electrochemical evaluation revealed that the nanocomposites containing 5 wt% of $Fe_{0.67}Cu_{0.22}Co_{0.11}S$ and 1 wt% of CuO (denoted as U5), exhibited a remarkable specific capacitance of 1407 F g^{-1} at 0.7 A g^{-1}, due to an optimal balance between redox active sulfides content and CuO-induced interfacial stabilization. Lower ratios such as 3 : 1 and 4 : 1 suffer from increased resistance caused by CuO as CuO forms stable heterointerfaces with FeCuCoS while higher ratio such as 6 : 1 lacks sufficient structural buffering and cannot retains its structure over long cycling In addition, the asymmetric supercapacitor device of similar electrodes showed superior energy density, power density, coulombic efficiency, and long-term cycling stability of 70 Wh kg^{-1}, 4800 W kg^{-1}, 97.1%, and 92.86% after 3000 cycles, respectively. Dunn's model and power-law fitting analysis indicated its hybrid supercapacitor behavior with dominance of capacitive nature, *i.e.*, 51.3% at 10 mV s^{-1}. Overall, U5 is a novel, durable, and high-performance material, which has great potential for utilization in advanced energy storage applications.

Author contributions

Muhammad Tariq: methodology, formal analysis, software, writing – original draft, data curation, Mohsin Ali Marwat: conceptualization, investigation, writing – review & editing, supervision, funding acquisition, project administration, Areeba Sajid: software, writing – original draft, visualization, Anusha Arif: formal analysis, writing – original draft, Zuhair Ehsan: formal analysis, writing – original draft, Muhammad Ramzan Abdul Karim: validation, writing – review & editing, Syed Shaheen Shah: validation, writing – review & editing.

Conflicts of interest

The authors declare that they have no known competing financial interests or personal relationships that could have appeared to influence the work reported in this paper.

Data availability

The data that supports the findings of this study are available upon reasonable request.

Supplementary information (SI) is available. See DOI: https://doi.org/10.1039/d5ra09004k.

Acknowledgements

M. A. Marwat acknowledges the valuable academic and research support from the Pakistan Science Foundation (PSF) Project No. PSF-NSFC/202307/19 and Ghulam Ishaq Khan (GIK) Institute of Engineering Sciences and Technology. Also, thanks for the financial support of the National Natural Science Foundation of China (No. 22461142142 and U24A20203).

References

1 A. D. Shuaibu, *et al.*, Advancing gel polymer electrolytes for next-generation high-performance solid-state supercapacitors: A comprehensive review, *J. Energy Storage*, 2025, **107**, 114851.
2 R. Sankannavar, *et al.*, A high-performance Ag@CoFe-layered double hydroxide supported on stainless steel mesh for solid-state energy storage, *J. Energy Storage*, 2025, **117**, 116185.
3 S. M. Abdullah, *et al.*, Tailoring NiCoCu layered double hydroxide with Ag-citrate/polyaniline/functionalized SWCNTs nanocomposites for supercapacitor applications, *RSC Adv.*, 2024, **14**(20), 14438–14451.
4 M. A. Marwat, *et al.*, High discharge energy density in rationally designed graphene oxide@ zinc oxide/polymer

blend-polyetherimide heterostructured bilayer nanocomposites, *J. Energy Storage*, 2024, **79**, 110125.
5 H. T. A. Awan, *et al.*, MXene-polymer hybrid composites for advanced energy storage: Insights into supercapacitors and batteries, *J. Energy Storage*, 2024, **95**, 112449.
6 X.-Y. Fu, *et al.*, Tag paper substrate enhanced self-assembled graphene oxide-Ti3C2Tx MXene composites for supercapacitors applications via laser processing, *J. Alloys Compd.*, 2025, **1010**, 178071.
7 S. Zhang, *et al.*, Flexible supercapacitors based on in-situ synthesis of composite nickel manganite@ reduced graphene oxide nanosheets cathode: An integration of high mechanical flexibility and energy storage, *J. Alloys Compd.*, 2024, **1009**, 176873.
8 A. Shuja, *et al.*, Supercapacitors for energy storage applications: Materials, devices and future directions: A comprehensive review, *J. Alloys Compd.*, 2024, **1009**, 176924.
9 M. A. Marwat, *et al.*, Enhancing supercapacitor performance of Ni–Co–Mn metal–organic frameworks by compositing it with polyaniline and reduced graphene oxide, *RSC Adv.*, 2024, **14**(3), 2102–2115.
10 H. Rong, *et al.*, Realizing higher-performance supercapacitor using three-dimensional cadmium-based coordination polymer, *J. Alloys Compd.*, 2025, **1010**, 177894.
11 M. Hussain, *et al.*, Hydrothermal synthesis of the NiS@ g-C3N4 nanohybrid electrode material for supercapacitor applications, *J. Energy Storage*, 2024, **80**, 110289.
12 M. S. Khan, *et al.*, Recent advancements in supercapacitors and their charge storage mechanism and progress in transition metal sulfide-based electrodes, *Phys. Scr.*, 2024, **99**(6), 062001.
13 G. Mirmoghtadaei, *et al.*, Ce-doped NiFe-layered-double-hydroxide hierarchical nanocomposite and metal/imidazolate framework carbon nanotube nanocomposite: A bifunctional material for OER electrocatalyst and supercapacitor electrode applications, *J. Alloys Compd.*, 2025, **1010**, 177377.
14 Z. M. El-Bahy, *et al.*, A novel DyCoO3@ rGO nanocomposite electrode material for hybrid supercapacitor devices, *J. Alloys Compd.*, 2025, **1010**, 178091.
15 Z.-Q. Wang, *et al.*, K-buserite manganese oxide nanosheets enabling high-efficiency energy storage in aqueous Zn-ion batteries and hybrid supercapacitors, *J. Energy Storage*, 2024, **75**, 109583.
16 L. Li, *et al.*, Recent Progress on Ruthenium-Based Electrocatalysts towards the Hydrogen Evolution Reaction, *Catalysts*, 2023, **13**(12), 1497.
17 L. Li, *et al.*, Strong electronic metal-support interaction of Ni4Mo/N-SrMoO4 promotes alkaline hydrogen electrocatalysis, *Appl. Catal., B*, 2025, **361**, 124660.
18 L. He, *et al.*, Single-atom Mo-tailored high-entropy-alloy ultrathin nanosheets with intrinsic tensile strain enhance electrocatalysis, *Nat. Commun.*, 2024, **15**(1), 2290.
19 X. Ren, *et al.*, Cationic vacancies and interface engineering on crystalline–amorphous gamma-phase Ni–Co oxyhydroxides achieve ultrahigh mass/areal/volumetric energy density flexible all-solid-state asymmetric supercapacitor, *J. Mater. Chem. A*, 2023, **11**(11), 5754–5765.
20 S. Ali, *et al.*, Ag NPs-modified NiCoMn layered double hydroxides electrodes for high-performance asymmetric supercapacitors, *J. Alloys Compd.*, 2024, **1008**, 176865.
21 P. Naskar, *et al.*, Chemical supercapacitors: a review focusing on metallic compounds and conducting polymers, *J. Mater. Chem. A*, 2021, **9**(4), 1970–2017.
22 B. Raut, *et al.*, Battery-type transition metal oxides in hybrid supercapacitors: Synthesis and applications, *Batteries*, 2025, **11**(2), 60.
23 R. Liang, *et al.*, Transition metal oxide electrode materials for supercapacitors: a review of recent developments, *Nanomaterials*, 2021, **11**(5), 1248.
24 M. Zhu, *et al.*, Recent advances in transition metal sulfide-based electrode materials for supercapacitors, *Chem. Commun.*, 2025, **61**(46), 8314–8326.
25 E. Ojegu and I. Ikhioya, Electrochemically Deposited Iron Sulphide Material by Adjusting the Deposition Time for Photovoltaic Application, *Phys. Access*, 2024, **4**, 55–63.
26 D. Han, *et al.*, Facile electrochemical conversion strategy for fabricating cobalt-based double metal sulfide nanosheets with high capacity and low electrochemical impedance, *J. Alloys Compd.*, 2024, **1007**, 176401.
27 Z. Huang, *et al.*, Bimetallic organic framework in situ fabrication nanoflower-like cobalt nickel sulfide and ultrathin layered double hydroxide arrays for high-efficient asymmetric hybrid supercapacitor, *J. Alloys Compd.*, 2023, **938**, 168565.
28 B. Shunmughananthan, *et al.*, Pseudocapacitive rare earth gallium oxides (RE3GaO6): A potential electrode family for asymmetric supercapacitors, *J. Alloys Compd.*, 2025, **1010**, 177749.
29 S. Ding, *et al.*, Heterogeneous layered bimetallic hydroxide electrode material for high-rate solid-state supercapacitor, *J. Alloys Compd.*, 2025, **1010**, 177985.
30 B. J. Rani, *et al.*, Supercapacitor and OER activity of transition metal (Mo, Co, Cu) sulphides, *J. Phys. Chem. Solids*, 2020, **138**, 109240.
31 S. Bhardwaj, *et al.*, Bimetallic Co–Fe sulfide and phosphide as efficient electrode materials for overall water splitting and supercapacitor, *Discover Nano*, 2023, **18**(1), 59.
32 R. Nivetha, *et al.*, Two-dimensional bimetallic Fe/M-(Ni, Zn, Co and Cu) metal organic framework as efficient and stable electrodes for overall water splitting and supercapacitor applications, *J. Energy Storage*, 2023, **61**, 106702.
33 C. Chen, *et al.*, Hierarchical NiCo-LDHs/metal sulfides (V3S4, CuS, Mo2S3) heterostructures with improved electrochemical properties for asymmetric supercapacitors: A comparative study, *J. Alloys Compd.*, 2024, **981**, 173682.
34 A. Patra, *et al.*, All-solid-state flexible supercapacitor based on a binary transition metal dichalcogenide grown on 2D/2D heterostructure materials, *J. Energy Storage*, 2023, **68**, 107825.
35 R. K. Devi, *et al.*, A facile strategy for the synthesis of manganese-doped nickel sulfide nanosheets and oxygen,

nitrogen-enriched 3D-graphene-like porous carbon for hybrid supercapacitor, *J. Alloys Compd.*, 2023, **944**, 169261.
36 M. Mondal, D. K. Goswami and T. K. Bhattacharyya, Flexible High-Energy-Density 4.3 V Supercapacitor Based on a Trimetallic Sulfide Cathode and a Bimetallic Sulfide-Polypyrrole Anode with an Ionic Liquid Gel Polymer Electrolyte, *ACS Appl. Electron. Mater.*, 2023, **5**(11), 6362–6383.
37 A. Patra, *et al.*, MoWS2 nanosheets incorporated nanocarbons for high-energy-density pseudocapacitive negatrode material and hydrogen evolution reaction, *Sustainable Energy Fuels*, 2022, **6**(12), 2941–2954.
38 X. Li, *et al.*, Core–shell structure trimetallic sulfide@ N-doped carbon composites as anodes for enhanced lithium-ion storage performance, *Molecules*, 2023, **28**(22), 7580.
39 R. Ullah, *et al.*, Elucidating bimetallic CuMnSe2/MWCNTs composite as redox-active electrode material for hybrid supercapacitors, *J. Energy Storage*, 2025, **109**, 115124.
40 N. A. Khan, *et al.*, Synergistic electrochemical performance of textile sludge based activated carbon with reduced graphene oxide as electrode for supercapacitor application, *Waste Manage.*, 2025, **191**, 274–283.
41 H. Hassan, *et al.*, Innovative Si@ MOF-5@ CNT hybrid: Tailoring energy storage and catalysis in batteries, supercapacitors, and hydrogen evolution, *Diamond Relat. Mater.*, 2024, **148**, 111507.
42 S. Mohammadi, *et al.*, High-capacity freestanding supercapacitor electrode based on electrospun Ti3C2Tx MXene/PANI/PVDF composite, *Heliyon*, 2024, **10**(22), e40482.
43 K. Batool, *et al.*, High electrochemical capacity of novel ternary graphene oxide based PANI/Co3O4 nanocomposite as supercapacitor electrode material, *Diamond Relat. Mater.*, 2024, **143**, 110904.
44 G. B. Pour, *et al.*, CNTs-supercapacitors: a review of electrode nanocomposites based on CNTs, graphene, metals, and polymers, *Symmetry*, 2023, **15**(6), 1179.
45 Y. Fang, *et al.*, Synthesis of copper-substituted CoS2@ CuxS double-shelled nanoboxes by sequential ion exchange for efficient sodium storage, *Angew. Chem., Int. Ed.*, 2020, **59**(7), 2644–2648.
46 Y. K. Jeong and G. M. Choi, Nonstoichiometry and electrical conduction of CuO, *J. Phys. Chem. Solids*, 1996, **57**(1), 81–84.
47 D. Majumdar, N. Baugh and S. K. Bhattacharya, Ultrasound assisted formation of reduced graphene oxide-copper (II) oxide nanocomposite for energy storage applications, *Colloids Surf., A*, 2017, **512**, 158–170.
48 H. Naderi-Samani, R. S. Razavi and R. Mozaffarinia, The effects of complex agent and sintering temperature on conductive copper complex paste, *Heliyon*, 2022, **8**(12), e12624.
49 B. Muthukutty, *et al.*, Multichannel Carbon Nanofibers: Pioneering the Future of Energy Storage, *ACS Nano*, 2024, **18**(40), 27287–27316.
50 P. Sathish Kumar, *et al.*, In-situ thermal reduction synthesis of porous carbon nitride doped gadolinium sulfide nanocomposite: An emerging electrode material for high-performance supercapacitor, *J. Energy Storage*, 2023, **74**, 109385.
51 J.-S. Kim and I.-H. Kim, Chalcopyrite CuFeS2: Solid-state synthesis and thermoelectric properties, *Materials*, 2024, **17**(22), 5497.
52 U. Hamayun, *et al.*, Synergistic integration of Ag@ Fe0. 67Cu0. 22Co0. 11S core-shell nanostructures and SWCNTs for improved supercapacitor performance, *J. Alloys Compd.*, 2025, **1012**, 178422.
53 S. Ramar, *et al.*, Morphological Tailoring of Transition Metal Tungstate Nanoreinforced Composite: A Key to Unlock High-Performance Supercapacitors, *Energy Fuels*, 2025, **39**(21), 10070–10082.
54 M. Amiri, *et al.*, Novel Rugby-Ball-like FeCoCuS2 Triple-Shelled Hollow Nanostructures with Enhanced Performance for Supercapattery, *Energy Fuels*, 2021, **35**(18), 15108–15117.
55 Q. Li, *et al.*, Unusual red light emission from nonmetallic Cu2Te microdisk for laser and SERS applications, *Adv. Opt. Mater.*, 2022, **10**(1), 2101976.
56 Y. Gao, *et al.*, Highly selective capacitive deionization of copper ions in FeS2@ N, S co-doped carbon electrode from wastewater, *Sep. Purif. Technol.*, 2021, **262**, 118336.
57 V. Sudha, G. Murugadoss and R. Thangamuthu, Structural and morphological tuning of Cu-based metal oxide nanoparticles by a facile chemical method and highly electrochemical sensing of sulphite, *Sci. Rep.*, 2021, **11**(1), 3413.
58 Y. Liu, *et al.*, Citrate esterification of debranched waxy maize starch: Structural, physicochemical and amylolysis properties, *Food Hydrocolloids*, 2020, **104**, 105704.
59 O. M. Yakymchuk, *et al.*, Effect of single-walled carbon nanotubes on tumor cells viability and formation of multicellular tumor spheroids, *Nanoscale Res. Lett.*, 2015, **10**(1), 150.
60 T. Abza, *et al.*, Characterization of cobalt sulfide thin films synthesized from acidic chemical baths, *Adv. Mater. Sci. Eng.*, 2020, **2020**(1), 2628706.
61 A. Varughese, R. Kaur, and P. Singh, Green synthesis and characterization of copper oxide nanoparticles using Psidium guajava leaf extract, in *IOP Conference Series: Materials Science and Engineering*, IOP Publishing, 2020.
62 G. Gottardi, *et al.*, Effects of oxygen concentration in the Ar/O2 plasma on the bulk structure and surface properties of RF reactively sputtered zirconia thin films, *Surf. Coat. Technol.*, 2008, **202**(11), 2332–2337.
63 M. Barazandeh and S. H. Kazemi, High-performance freestanding supercapacitor electrode based on polypyrrole coated nickel cobalt sulfide nanostructures, *Sci. Rep.*, 2022, **12**(1), 4628.
64 U. Aziz, *et al.*, Exploring the redox activity of a transition-metal-intercalated 1, 3, 5-benzenetricarboxylic acid organic–inorganic network for potential battery–supercapacitor applications, *Energy Fuels*, 2023, **37**(8), 6248–6256.
65 P. S. Kumar, *et al.*, Enhanced voltage and capacitance in flexible supercapacitors using electrospun nanofiber

electrolytes and CuNi2O3@N-Doped omnichannel carbon electrodes, *Nano Convergence*, 2025, **12**(1), 21.

66 M. A. Karim, *et al.*, Electrochemical insights into NiCoCu-based MOFs for energy storage applications, *Electrochim. Acta*, 2025, **542**, 147509.

67 X. Yang, *et al.*, 3D hierarchical NiCo2S4 nanoparticles/carbon nanotube sponge cathode for highly compressible asymmetric supercapacitors, *Energy Fuels*, 2021, **35**(4), 3449–3458.

68 J. Zhao and A. F. Burke, Review on supercapacitors: Technologies and performance evaluation, *J. Energy Chem.*, 2021, **59**, 276–291.

69 X. Li, *et al.*, Preparation of a hollow cube NiCo2S4 and its application in supercapacitor, *J. Chem. Sci.*, 2020, **132**(1), 101.

70 R. Singhal, *et al.*, Synthesis and characterization of CuS, CuS/graphene oxide nanocomposite for supercapacitor applications, *AIP Adv.*, 2020, **10**(3), 035307.